Heating efficiency of Gd- and Co-doped γ-Fe_2O_3 nanoparticles measured by AC magnetometer for magnetic-mediated hyperthermia.

O. M. Lemine,[1*] Kheireddine El-Boubbou,[2,3,4] Inaki Orue,[5] José Ángel García,[6] M. Elansary,[7] Rizwan Ali[3] and L. El Mir[8] and M Henini[9]

[1]Department of Physics, College of Science, Imam Mohammad Ibn Saud Islamic University (IMISU), Riyadh 11623, Saudi Arabia

[2]Department of Chemistry, College of Science, University of Bahrain, Sakhir 32038, Bahrain

[3]King Abdullah International Medical Research Center (KAIMRC) & King Saud bin Abdulaziz University for Health Sciences (KSAU-HS), King Abdulaziz Medical City, National Guard Health Affairs, Riyadh 11426, Saudi Arabia

[4]Nanomaterials for Bioimaging Group (nanoBIG), Facultad de Ciencias, Departamento de Física de Materiales, Universidad Autónoma de Madrid (UAM), Madrid 28049, Spain

[5]SGIker Medidas Magnéticas, Universidad del País Vasco (UPV/EHU), 48940 Leioa, Spain

[6]Departamento de Física, Universidad del País Vasco (UPV/EHU), 48940 Leioa, Spain

[7]Nanoscience and Nanotechnology Unit, E.N.S Rabat, Energy Research Centre. Mohammed V University, B.P. 5118, Takaddoum Rabat, Morocco

[8]Laboratory of Physics of Materials and Nanomaterials Applied at Environment, Faculty of Sciences of Gabes, University of Gabes, 6072 Gabes, Tunisia

[9]School of Physics and Astronomy, University of Nottingham, Nottingham, NG7 2RD, UK

[*]Corresponding author: O. M. Lemine (E-mail: mamamin@imamu.edu.sa; Tel: +966 112594627)

Abstract

Most research groups, including us, utilize calorimetric methods to determine the heat dissipation by magnetic nanoparticles (MNPs) under an alternating magnetic field (AMF). Herein, we report the heating efficiencies of γ-Fe2O3 and doped γ-Fe_2O_3 NPs using AC magnetometry, which allows us to directly calculate the AC hysteresis loop area from which the heating abilities can be deduced. First, all NPs were prepared and thoroughly characterized both structurally (XRD, Rietveld, and TEM) and magnetically (DC and AC magnetization measurements). Structural analysis indicated the phase purity (γ-Fe2O3) and crystallite sizes (~ 10 nm) of the as-prepared γ-Fe_2O_3 NPs. Both DC and AC measurements indicated the superparamagnetic behavior for γ-Fe_2O_3 and Gd-doped γ-Fe_2O_3(Gd-5%) NPs, while Co-doped γ-Fe_2O_3(Co-5%) NPs exhibited ferrimagnetic nature. The heating abilities and specific absorption rate (SAR) values were then analyzed at frequency, f = 132 kHz and several AC field amplitudes ($\mu_0 H_{AC}$) ranging from 0 to 88 mT. From AC

magnetometry calculations, the SAR values were found to be 20 W/g and 17 W/g for γ-Fe_2O_3 and γ-Fe_2O_3(Gd-5%) NPs, respectively, while that of γ-Fe_2O_3(Co-5%) NPs reached SAR of 120 W/g, almost 6 times higher. This high heating efficiency of γ-Fe_2O_3(Co-5%) sample is attributed to their higher effective anisotropy and saturation magnetization where the heat release is mainly dominated by Neel relaxation. Finally, a viability assay against metastatic breast cancer cells was conducted, indicating the biocompatibility and low toxicity of the as-synthesized γ-Fe_2O_3 and doped γ-Fe_2O_3 NPs. These results strongly suggest the promising utilization of γ-Fe_2O_3 NPs, particularly Co-doped, as a potential candidate for magnetic-mediated hyperthermia.

1. Introduction

The utilization of magnetic nanoparticles (MNPs) as a source of heat in magnetic fluid hyperthermia (MFH) is currently attracting much attention due to its remarkable hyperthermia therapeutic effects [1-3]. For efficient hyperthermia therapy, it is crucial to optimize their heating efficiency signified by the value of sample absorption rate (SAR), defined as the absorbed energy per unit gram of magnetic material and per unit time [4]. The main challenge lies in obtaining MNPs of particular characteristics (i.e. Curie temperature in the range 42 – 46 °C and large SAR values). As proved by many previous reports [4-8], SAR values are affected by magnetic properties, size, shape, interactions between particles, which influence the magnetic moment rotation responsible of heat dissipated through Brownian and Néel relaxation mechanisms. Additionally, SAR should be optimized by using minimal dosage of the MNPs (to ensure biocompatibility), where the frequency and field amplitude chosen should satisfy medical safety condition ($H_0 \times f \leq 5 \times 10^9$ A/m.s) [9].

Most research groups, including us, employ calorimetric methods to determine SAR values, by measuring the temperature rise as a function of time when MNPs are exposed to AMF [5-8]. The SAR is then calculated by using the following equation:

$$SAR = \frac{\rho C_w}{Mass_{MNP}} \left(\frac{\Delta T}{\Delta t}\right) \quad (1)$$

where C_w is defined as the specific heat capacity of water (4.185 J/g.k), the density of the colloid is ρ, the concentration of the magnetic nanoparticles in the suspension is called $Mass_{MNP}$ and the heating rate is represented by $\frac{\Delta T}{\Delta t}$. However, as shown in equation (1), there are several factors that can affect the accuracy of SAR values. For example, Wang el al. [10] reported that a large error occurs with a longer heating time and higher power level when calculating initial temperature slope. Recently, we observed that doping γ-Fe_2O_3 with 1- 5% Cobalt (Co) did not increase the

SAR values compared to undoped γ-Fe_2O_3, instead the high saturation and magnetic anisotropy constant [9]. It was found that difficulties in obtaining a very stable colloidal suspension directly affected the obtained values of SAR. Consequently, an alternative method to determine SAR values using the AC magnetometry was proposed by other researchers [11-15]. It is well known that heat dissipated by MNPs under AC magnetic fields is originated by the hysteretic dynamic responses of these MNPs to the AC field and can be calculated by:

$$SAR = f \times A \quad (2)$$

where f and A are the frequency and the area of the hysteresis, respectively. Thus, AC magnetometer allows a direct determination of the hysteresis area.

Taking all these facts into consideration, we, herein, evaluated the self-heating abilities of γ-Fe_2O_3, Gd-doped γ-Fe_2O_3(Gd-5%) and Co-doped γ-Fe_2O_3(Co-5%) using AC magnetometry. We systematically investigated the effects of changing field amplitude on SAR values and studied their magnetic response with DC magnetometry.

2. Materials and Methods

2.1. Materials

Unless otherwise indicated, all chemicals and solvents were obtained from commercial suppliers and used as supplied without further purification. iron (III) acetylacetonate. Phosphate Buffered Saline (PBS), Advanced Dulbecco's Modified Eagle Medium (DMEM), Phenol-red free DMEM, Fetal Bovine Serum (FBS), and Penicillin-Streptomycin (Pen-Strep) were all purchased from UFC Biotechnology. MTT (Thiazolyl Blue Tetrazolium Bromide) powder was purchased from Bioworld, USA. Human metastatic cancer cell lines were purchased from American Type Culture Collection (ATCC) and grown in DMEM supplemented with 10% FBS and 1% Penicillin/Streptomycin. The cancerous cells used in this study are MDA-MB-231 (metastatic breast cancer cell line isolated at MD Anderson from a pleural effusion of a 51-year-old Caucasian woman with invasive ductal carcinoma).

2.2. Preparation and Characterization

Undoped and doped γ-Fe_2O_3 were synthesized as in our previous reports [9, 16], using a modified sol-gel process under supercritical conditions of ethanol and iron (III) acetylacetonate as the iron precursor. The samples are denoted as γ-Fe_2O_3, Gd-doped γ-Fe_2O_3(Gd-5%) and Co-doped γ-Fe_2O_3(Co-5%) based on percentage of doping.

XRD analysis was performed by Using Bruker D8 Discover diffractometer (θ-2θ) equipped with Cu-Kα radiation (λ=1.5406 Å). The average crystallite size is deduced from the X-ray diffractograms by Scherrer formula (3) [16]:

$$D = \frac{K\lambda}{\mathrm{B}\ \cos(\theta)} \quad (3)$$

where λ = 1.54178 Å, D crystallite size, K is a constant whose value is approximately 0.9 and B (rad) is the full width at half maximum (FWHM) of a diffraction peak.

TEM images were collected on a JEOL-JEM 1400 operating at 120 kV using Gatan camera with Digital Micrograph Imaging software. Samples were prepared by depositing 5 µl of the MNP aqueous dispersion onto 75 mesh Formvar/Carbon-supported copper grids. The suspension was then allowed to air dry before images were taken. DC magnetization (M) measurements were performed at room temperature using a Quantum Design QD-MPMS (SQUID) magnetometer. AC magnetometry measurements were performed using a home-made magnetometer developed by Rodrigo et al. [15]. This system can work at a wide frequency range (100 kHz - 1 MHz) with large field intensity: 90 mT at low frequency side and 35 mT at high frequency side.

2.2.Cytotoxicity Assay.

The 3-(4,5-dimethylthiazol-2-yl)-2,5-diphenyl-2H-tetrazolium bromide (MTT) assay was utilized to examine the anti-proliferative activity of γ-Fe_2O_3, Gd-doped γ-Fe_2O_3, and Co-doped γ-Fe_2O_3 NPs against triple-negative breast cancer cell lines, MDA-MB-231. The cells were seeded at a density of $5x10^3$ cells/well in a 96-well plate overnight. Later, the cells were treated with varying concentrations of each NPs sample ranging from 0 to 500 µg/ml. Following a 24 hr incubation period at 37 °C and 5% CO_2, MTT solution (5 mg/ml) was added to each well. The MTT solution was aspirated post 3 hrs and 100ul of DMSO was then added. After 45 minutes of incubation at 300-rpm shaker, the absorbance was measured at OD = 590 nm. The percentage of viable cells was calculated as the ratio of the absorbance of the treated group, divided by the absorbance of the control group, multiplied by 100. The absorbance from the untreated control cells was set as 100% viable. All the experiments were carried out in triplicate.

3. Results and Discussion

3. 1. Structural and magnetic characterization

X-ray diffractograms of γ-Fe_2O_3, γ-Fe_2O_3(Gd-5%) and γ-Fe_2O_3(Co-5%) NPs are shown in **Fig. 1.** The diffractograms of Fe_2O_3 NPs indicated the presence of diffraction peaks which correspond to

cubic structure, which could be indexed based on γ-Fe_2O_3 with space group P4132 (JCPDS No. 39-1346). No additional peaks have been observed after doping suggesting that our synthetic method leads to the formation of a pure phase of γ-Fe_2O_3. The absence of secondary phases in the X-ray diffractograms indicated that Gd^{+3} and Co^{+2} ions are incorporated in the lattice.

However, it is important to highlight the difficulty of differentiating between the two phases form the X-ray diffractograms due to their structural similarities [17]. Thus, other techniques such as Mössbauer spectroscopy should be used for distinguishing between the two phases. Since the hyperfine parameters of both Fe-oxides are different: the spectrum corresponding to γ-Fe_2O_3 is characterized by two asymmetrical resolved sextets for the Fe3+, whereas magnetite spectrum shows two well resolved sextets corresponding to Fe^{3+} at the tetrahedral sites (33%) and the $Fe^{3+}$and Fe^{2+} at the octahedral sites, respectively [6]. Our previous works [6,18] on Mössbauer spectroscopy at room temperature showed that hyperfine parameters are very close to γ-Fe_2O_3 phase indicating that the synthesized phases could be indexed as γ-Fe_2O_3.

Rietveld refinement was performed as shown in **Fig. 2**, where all diffraction peaks can be indexed to the cubic structure of γ-Fe_2O_3 with space group P4132 N° 213. The quality of refinement was judged by the reliability factor (χ^2). A better fit is obtained for where (χ^2<1.5). It is important to note that some diffraction peaks do not refine perfectly due to the internal structure of $\gamma -Fe_2O_3$, particularly in the presence of the doping elements Gd^{3+} and Co^{2+}. The introduction of these doping elements can lead to local deformations or residual stresses, which can alter the interatomic distances from those of the ideal crystalline material. These local variations can have an impact on the quality of refinement of experimental X-ray diffractograms data. The values of the refined lattice parameters, the lattice volume (v) and the average crystallite sizes are summarized in **Table 1**. As can be observed, the lattice parameter is increased by doping. This increase is due to the different value of ionic radius of Fe^{3+} (0.65 nm) comparable to the doping elements Co^{2+} (0.74 nm) and Gd^{3+} (0.93 nm). Doping with Co^{2+} and Gd^{3+} also increases the average crystallite sizes, particularly for the sample doped with Gd ions. Previous reports show that the doping by rare-earth elements increases the sizes of crystallites because the energy of formation of the bonds of rare earth are greater than the energy of the transition metals $\Delta H(Gd - O) = 715\ Kj.mol^{-1}$, $\Delta H(Fe - O) = 407\ Kj.mol^{-1}$ and $\Delta H(Co - O) = 397\ Kj.mol^{-1}$ [19]. The increase observed in the crystallite size might be due to the nanoscale structural nature of $\gamma - Fe_2O_3$ $\left\{(Fe^{3+})_8 \left[Fe^{3+}_{5/3}\ \boxdot_{1/3}\right]_8 O_{32}\right\}$ Fe vacancy site (⊡), where probably Gd^{3+} is inserted in the grain boundaries.

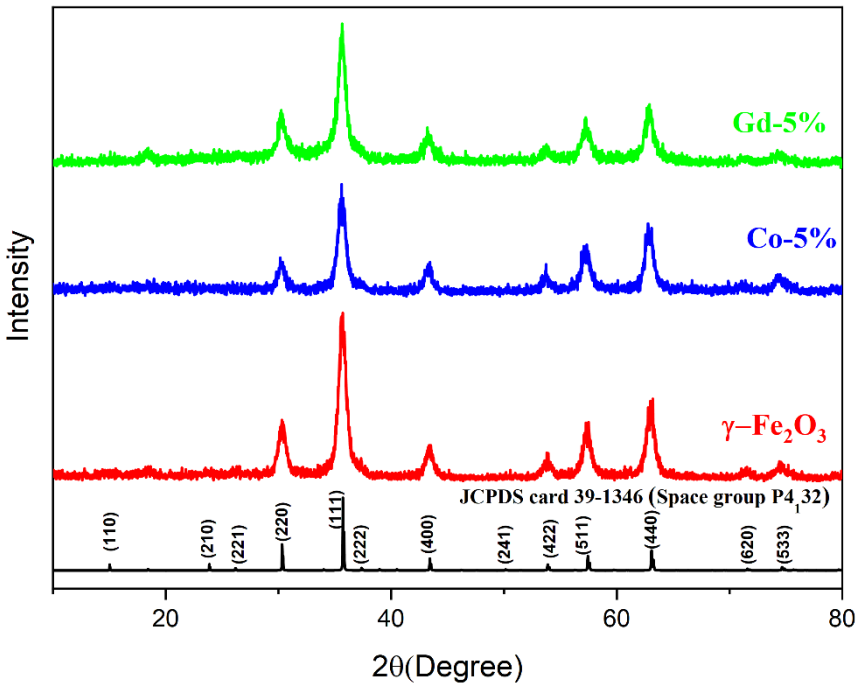

Fig. 1 Powder X-ray diffractograms of γ-Fe_2O_3, Co-doped γ-Fe_2O_3(Co-5%) and Gd- doped γ-Fe_2O_3(Gd-5%)

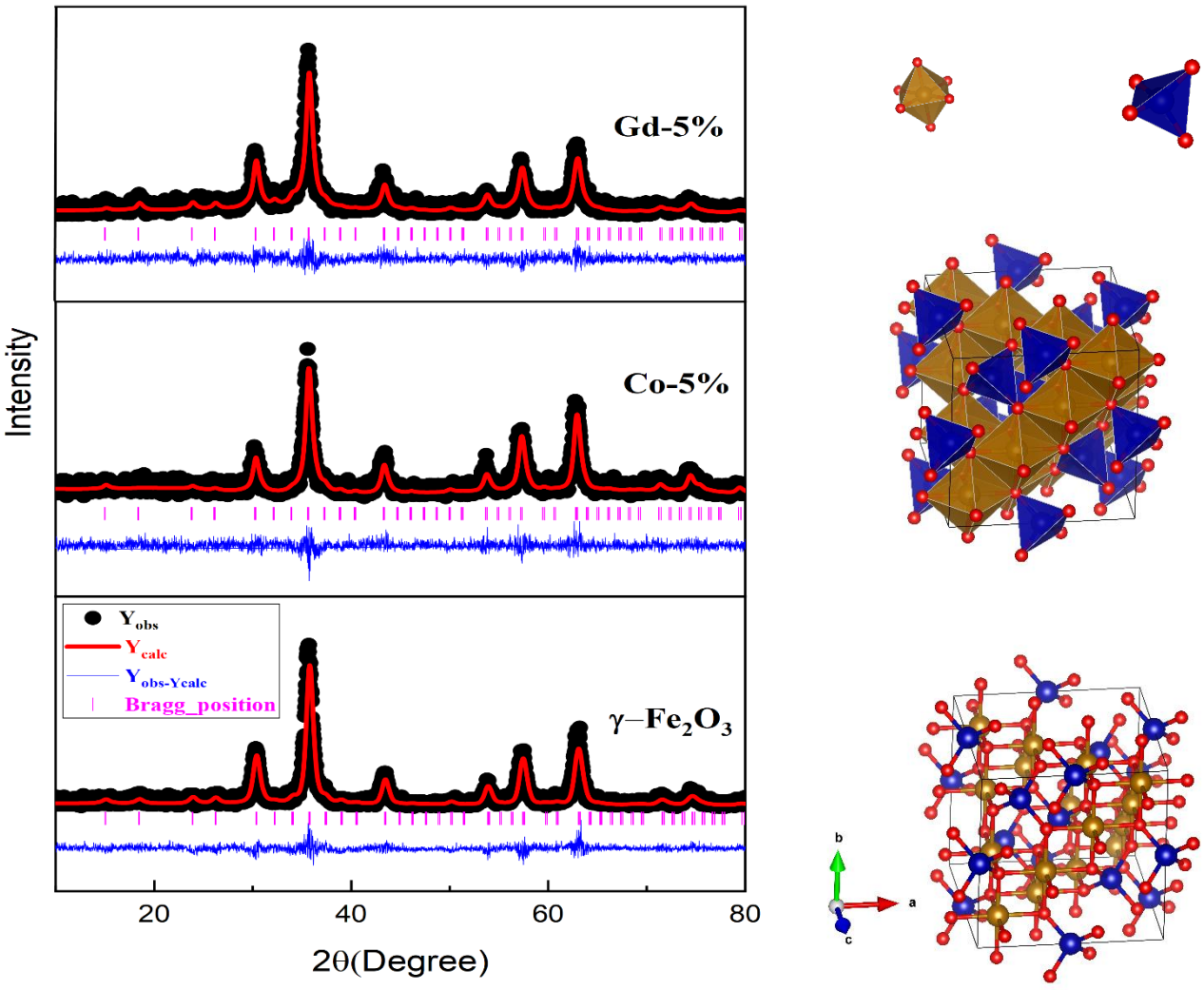

Figure.2 Rietveld refinement of X-ray diffractograms of samples using Full-Prof software

Table.1 The calculated values of the lattice parameter (a), cell volume and the crystallite size.

Samples	a (Å)	Cell volume ($Å^3$)	Crystallite sizes (nm)
γ-Fe_2O_3	8.346	581.346	12
γ-Fe_2O_3 (Co-5%)	8.357	583.790	13
γ-Fe_2O_3(Gd-5%)	8.373	587.214	21

Fig. 3. showed TEM images of the different samples. The core size distributions of γ-Fe_2O_3, Co-doped γ-Fe_2O_3(Co-5%) and Gd-doped γ-Fe_2O_3(Gd-5%) MNPs were found to be between 5 and 15 nm, mainly centred at ~ 9 nm. Generally, the uniformity, quasi-spherical morphology, and narrow size distribution are well depicted from all the TEM images. As expected, the narrowest size distribution was observed for pure γ-Fe_2O_3, and widens as the nanoparticles become doped with Co or Gd. Moreover, these calculated particle size distributions fit well with the range of the grain sizes obtained from XRD calculations, showing the biggest crystallite sizes for Gd-doped γ-Fe_2O_3 sample.

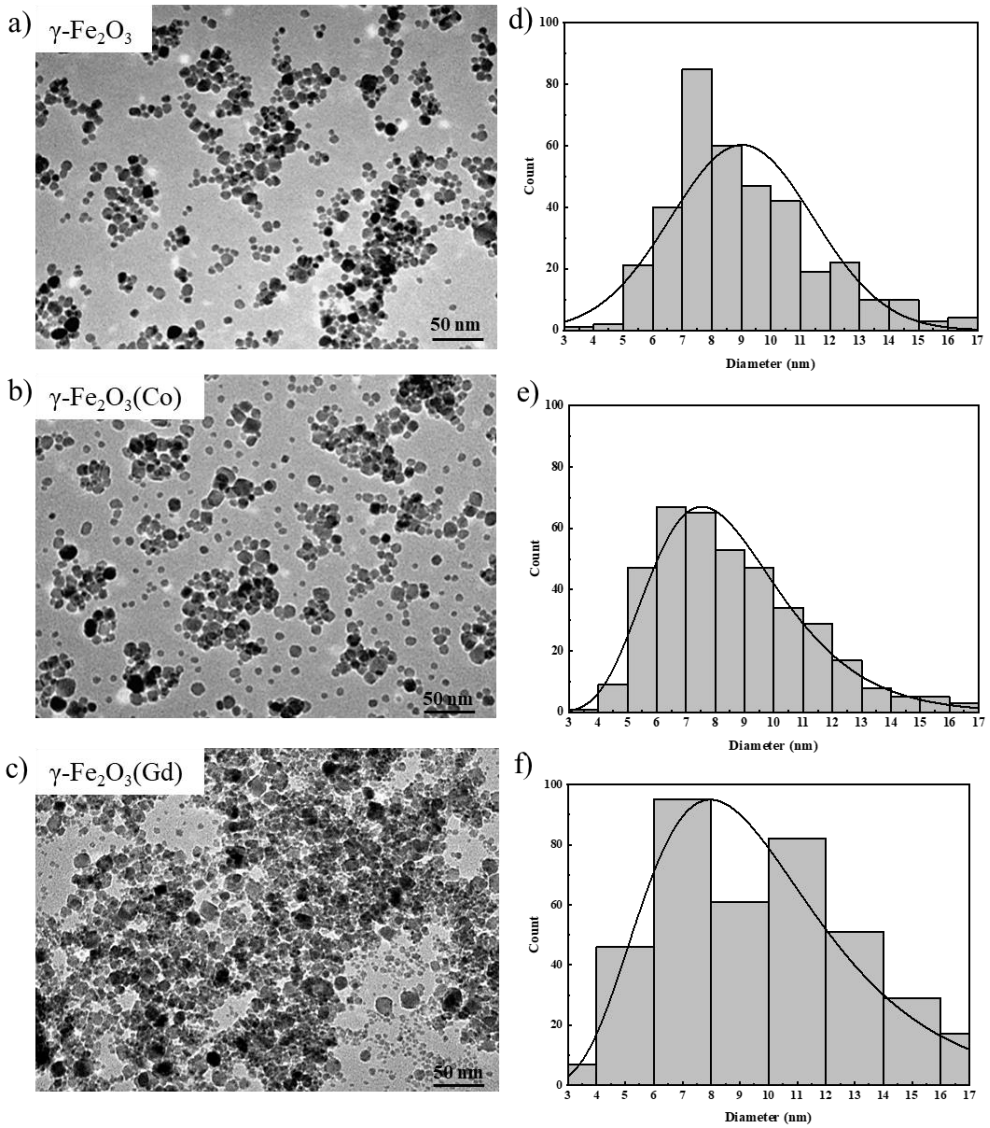

Fig. 3. (a-c) TEM images of the different samples a) γ-Fe_2O_3, b) Co-doped γ-Fe_2O_3(Co-5%) and c) Gd-doped γ-Fe_2O_3(Gd-5%) MNPs, along with their (d-f) corresponding particle-size distributions.

Fig. 4a depicted the hysteresis loop (M–H) at room temperature for γ-Fe_2O_3, γ-Fe_2O_3(Gd-5%) and γ-Fe_2O_3(Co-5%) NP, while table.2 summarized the magnetic parameters. As can be observed from the M-H curves at low field (inset Fig. **4b**), γ-Fe_2O_3 and γ-Fe_2O_3(Gd-5%) NPs have negligible coercivity and remanence indicating a superparamagnetic behavior. γ-Fe_2O_3(Co-5%) NPs, however, behaves as ferrimagnetic, where the remanence and coercivity are 0.012 T and 6.77 A.m^2/kg, respectively. The superparamagnetic behavior of γ-Fe_2O_3 and γ-Fe_2O_3(Gd-5%) NPs is confirmed by the successful fitting of the experimental magnetization at room temperature with Langevin's theory of paramagnetism as shown in **Fig. 4b**. The magnetization of non-interacting superparamagnetic particles in an external magnetic field (H) can be described by the following Langevin function:

$$M = M_s \left(\coth\left(\frac{m_{np}H}{K_BT}\right) - \frac{K_BT}{m_{np}H}\right) \quad (4)$$

where $M_s$is the saturation, m_{np} is the magnetic moment of the NP, T is the temperature (300 K), and K_B is the Boltzman constant. Furthermore, we determined the mean particle size diameter of γ-Fe_2O_3 and γ Fe_2O_3(Gd-5%) by using the following expression [20],

$$m_{np} = \frac{\pi d^3 M_s}{6} \quad (5)$$

where m_{np} and M_s are determined from the fitting. It was found the average particle size is around 10 nm for the two samples, which is comparable to the size deduced from TEM images.

Moreover, the saturation values were obtained by fitting the experimental magnetization with law of approach to saturation (LAS) as depicted in the equation (6) [21],

$$\mathrm{M(H)} = \mathrm{M_s}\left(1 - \frac{\mathrm{b}}{\mathrm{H^2}}\right) \quad (6)$$

This allows us to characterize the magnetization close to saturation. Guivar et al. used similar approach based on LAS in their elegant work dedicated to the functionalized γ-Fe_2O_3 nanoparticles [22]. As expected, Co-doped γ-Fe_2O_3 has the highest saturation (63.7 A.m^2/kg), while in Gd-doped γ-Fe_2O_3 the saturation is reduced from 52.3 A.m^2/kg to 45.77 A.m^2/kg.

Regarding the increase of saturation of Co-doped γ-Fe_2O_3 NPs, it might be due to the incorporation of Co ions in γ-Fe2O3 sites. The interaction between Co ions spin and the lattice favors the alignment of Co^{2+} spins parallel to the cube edge of the spinel lattice. In addition, the cobalt ions will induce uniaxial magnetic anisotropy in the magnetization direction and will increase saturation. The decrease of saturation observed for γ Fe_2O_3(Gd-5%) can be explained by the insertion of large Gd ions in the octahedral sites in γ-Fe2O3 . This will affect Fe-Gd interactions

and induce decrease in long range magnetic ordering. Furthermore, Gd^{3+} has properties of weak magnetic anisotropy, which can lead to reduced stability of aligned magnetic domains in the material, thus contributing to a decrease in saturation magnetization.

	M_s (emu/g)		
Samples	**Experimental**	**Langevin method**	**Law of approach to saturation (LAS),**
γ-Fe_2O_3	52.13	53.61	53.68
γ-Fe_2O_3 (Gd-5%)	39.35	40.61	40.71
γ-Fe_2O_3(Co-5%)	66.73	67.49	66.95

Table.2 Saturation at room temperature deduced from experimental, Langevin fitting and LAS

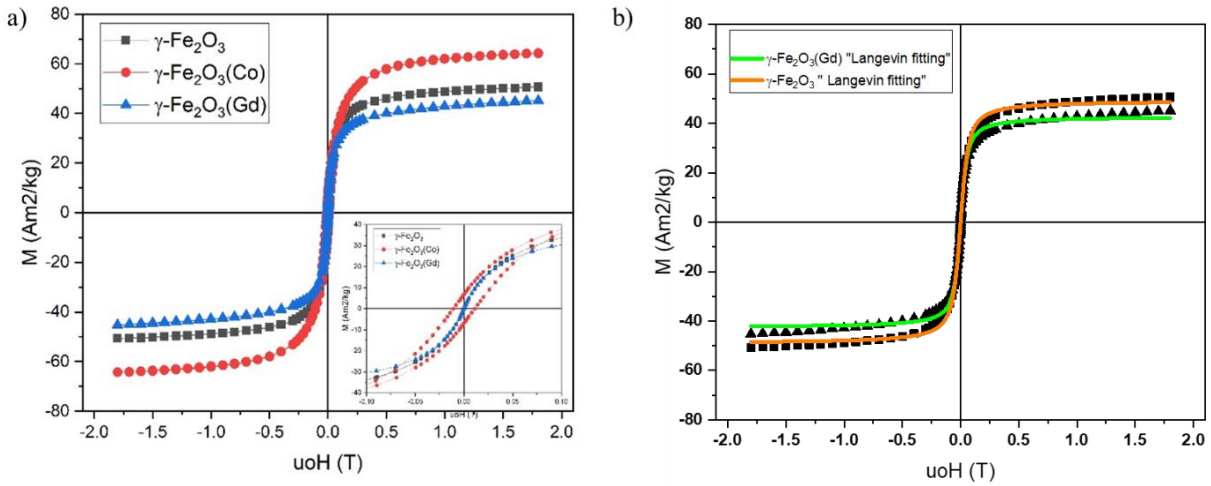

Fig. 4. (a) M-H curves at room temperature and (b)Fitting of the experimental magnetization with Langevin function.

3.2. Magnetic hyperthermia measurements

In our previous reports, we reported the heating efficiencies of MNPs using calorimetric method as a function of concentration, frequency, and field amplitude [9, 16]. It was found that all the samples show good heating abilities and reach magnetic hyperthermia temperature (42 °C) in a relatively short time. However, these studies show the necessity to use relatively high value of the applied field amplitude (limited value by calorimetric method), as well as the necessity of reducing the error sources in the calculation of SAR values. Thus, AC magnetometry measurements are used herein instead, which allow us to measure the AC hysteresis loop area and from this area, the heating abilities will be deduced.

As shown in **Fig. 5**, the AC loops were measured at frequency, f = 132 kHz and for different AC field amplitude ($\mu_0 H_{AC}$) ranging from 0 to 88 mT. As can be observed, γ-Fe_2O_3 and γ-Fe_2O_3(Gd-5%) NPs show negligible coercivity and remanence instead of the high AC field amplitude indicating their superparamagnetic behavior and corroborating the DC magnetization results. The high AC field amplitude does not induce an hysteresis due that the particle are too small and the magnetic anisotropy also. γ-Fe_2O_3(Co-5%) NPs shows hysteresis losses where the AC loops become larger as the field amplitude increases. Furthermore, the areas under the curves increased with increasing applied field for γ-Fe_2O_3(Co-5%) NPs, while undoped and Gd doped γ-Fe2O3 displayed an almost perfectly reversible hysteresis loop.

Quantitative analysis based on the areas of the loops allows the calculation of SAR by using the following equation:

$$SAR = \frac{f}{c}.A = \frac{f}{c}\oint \mu_0 M_t dH_t \quad (7)$$

where M_t is the instantaneous magnetization at time t, H_t the sinusoidal magnetic field of frequency f at time t, and c is the magnetic material weight [15]. SAR values as function of AC field amplitude for the three samples are depicted in **Fig. 6.(a)** As can be noticed, and as expected, γ-Fe_2O_3 and γ-Fe_2O_3 (Gd-5%) NPs exhibited very low SAR, while γ-Fe_2O_3(Co-5%) showed the highest SAR values. The calculated SAR values ($\mu_0 H_{AC}$ = 88 mT) were found to be 20 W/g and 17 W/g for γ-Fe_2O_3 and γ-Fe_2O_3 (Gd-5%) NPs, respectively. Remarkably, at the same AC field amplitude, γ-Fe_2O_3(Co-5%) NPs reached SAR of 120 W/g.

Generally, SAR depends on many parameters such as size, crystallinity, saturation, and magnetic anisotropy constant [5]. When the size and crystallinity of MNPs are comparable, their effect can be excluded. Thus, the difference in the observed heating ability of the different MNPs could be understood in terms of saturation and magnetic anisotropy constant (K_{eff}). The saturation deduced from DC measurements depicted high value for Co-doped γ-Fe_2O_3. On the other hand, our previous reports [9,16] indicated a higher value of magnetic anisotropy constant for γ-

Fe_2O_3(Co-5%) NP (0.2 $\times 10^5$ J/m^3) compared to that for γ-Fe_2O_3 (0.15 $\times 10^5$ J/m^3) and γ-Fe_2O_3(Gd-5%) (0.091x10^5 J/m^3) NPs. Therefore, we can conclude that the high heating ability of γ-Fe_2O_3 (Co-5%) NP is due mainly to their high saturation (M_s) and the effective anisotropy constant (K_{eff}).

Further analysis of SAR values can be performed based on the linear response theory and as reported by Morales et al.[24] in their elegant work. In this model, SAR varies linearly as a function of square of field amplitude and given as below [6]:

$$SAR = c f H^2 \quad (8)$$

where c is a constant, f is the frequency and H is amplitude of the field.

It can be seen clearly from **Fig.6(a)** that field amplitude dependence of experimental SARs has a quadratic behavior with the field before 50mT as expected by the LRT model. Above a 50 mT, the SAR is almost saturated. This behavior is more pronounced for γ-Fe_2O_3 and γ-Fe_2O_3 (Gd-5%) **(Fig.6(b)** due to their superparamagnetic beahvior

Regarding the mechanism responsible for the heat dissipated by these NPs under AMF, given that samples are measured as solid due to the difficulty to obtain stable colloidal suspension, the heat is emit through Néel relaxation.

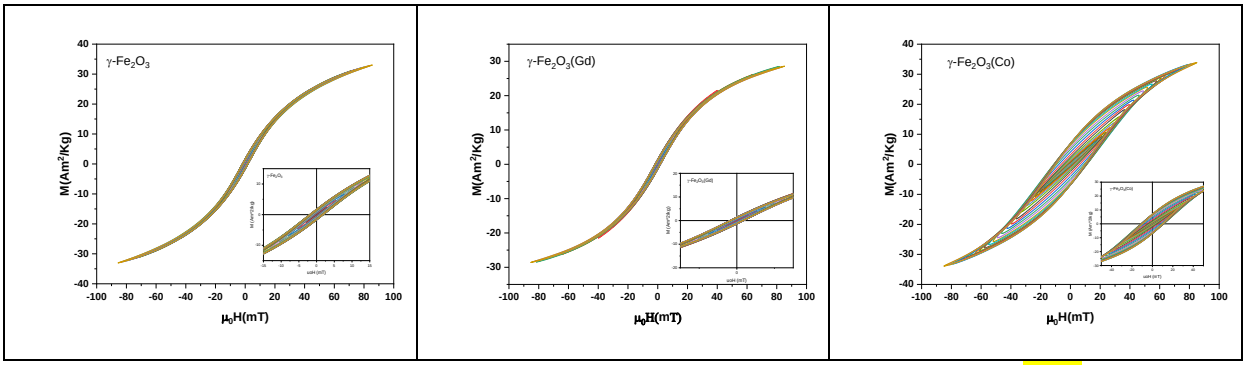

Fig. 5. Hysteresis loops measured at frequency, f = 132 kHz and at different AC field amplitudes.

a)	**b)**

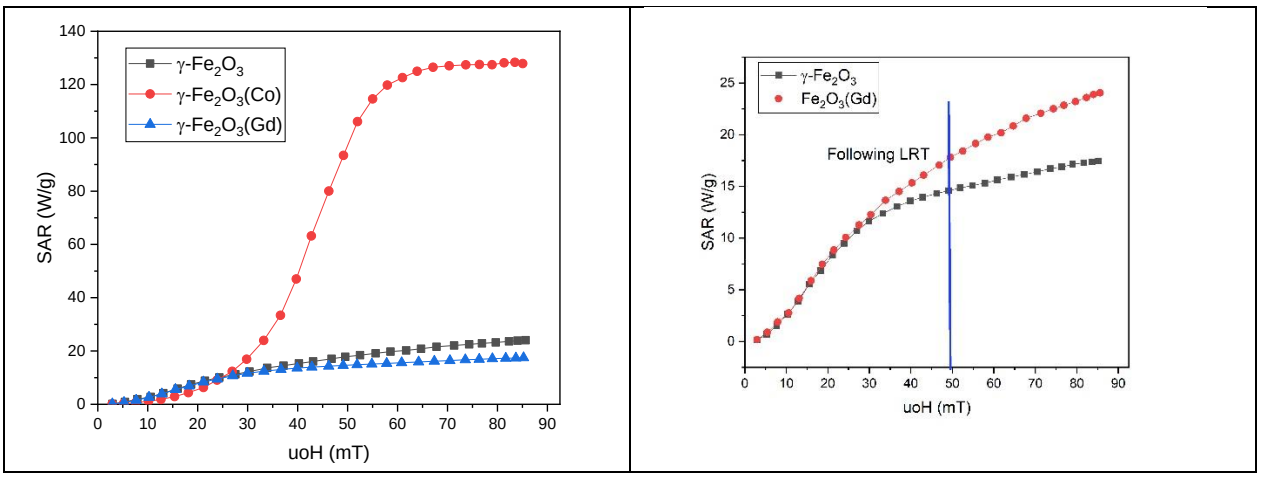

Fig. 6. SAR values for the different samples as function of AC field amplitude ($\mu_0 H_{AC}$ = 0 - 88 mT) and at frequency, f = 132 kHz.

Finally, comparison of the heating ability of our NPs with other systems through the SAR values is depicted in **Table 3**. But this comparison of SAR values does not give much information on the heating efficiency given that each study have its own experimental conditions such as concentration, magnetic properties, field amplitude, frequency etc.

Table 3. Comparison of SAR values for different magnetic NPs

Magnetic nanoparticles	Synthesis method	Frequency (kHz)	Field (mT)	SAR (W/g)	Ref
γ-Fe_2O_3	Modified Sol-gel	113	85	20	This work
Gd-γ-Fe_2O_3	Modified Sol-gel	113	85	17	This work
Co-γ-Fe_2O_3	Modified Sol-gel	113	85	125	This work
Gd -Fe_2O_3	Sol-gel	332	17	40	[16]
Fe3O4	Hydrothermal	332	17	17.32	[8]
Co -Fe_2O_3	Sol-gel	332	17	60	[9]

3.3. Biocompatibility of various γ-Fe_2O_3 MNPs

For successful cancer magnetic hyperthermia treatment, it is important that the utilized MNPs generate the maximum temperature increase at the lowest possible concentration and within a clinically relevant AC magnetic field (Hergt's limit $H_0 f < 5 \times 10^9$ A/m^{-1}s^{-1}). Thus, it is essential to assess the potential toxicity of the as-synthesized NPs before utilizing them for magnetic hyperthermia applications. In this study, the cytotoxicity of the different samples (γ-Fe_2O_3, Co-doped γ-Fe_2O_3, and Gd-doped γ-Fe_2O_3 NPs) was evaluated on a metastatic breast cancer cell line, MDA-MB-231, using the thiazolyl blue tetrazolium bromide (MTT) viability assay. As depicted in **Fig. 7**, γ-Fe_2O_3 and Co-doped γ-Fe_2O_3 MNPs did not exhibit significant toxicity towards MDA-MB-231 metastatic cancer cells (~ 80% of the cells remained viable), even at the high concentrations tested (up to 50 µg/mL). The cell viability was slightly decreased for Gd-doped γ-Fe_2O_3 MNPs, but it is still acceptable taking into consideration the toxic characteristics of the rare-earth metal Gd [23]. These findings align well with previous studies conducted by us and others, demonstrating the safety of γ-Fe_2O_3 and γ-Fe_2O_3 doped MNPs for biomedical applications [25,26]. Combined with the high heating efficiencies and SAR values obtained (120 W/g), our results strongly indicate the promising potential of Co-doped γ-Fe_2O_3 MNPs for magnetic-mediated hyperthermia applications.

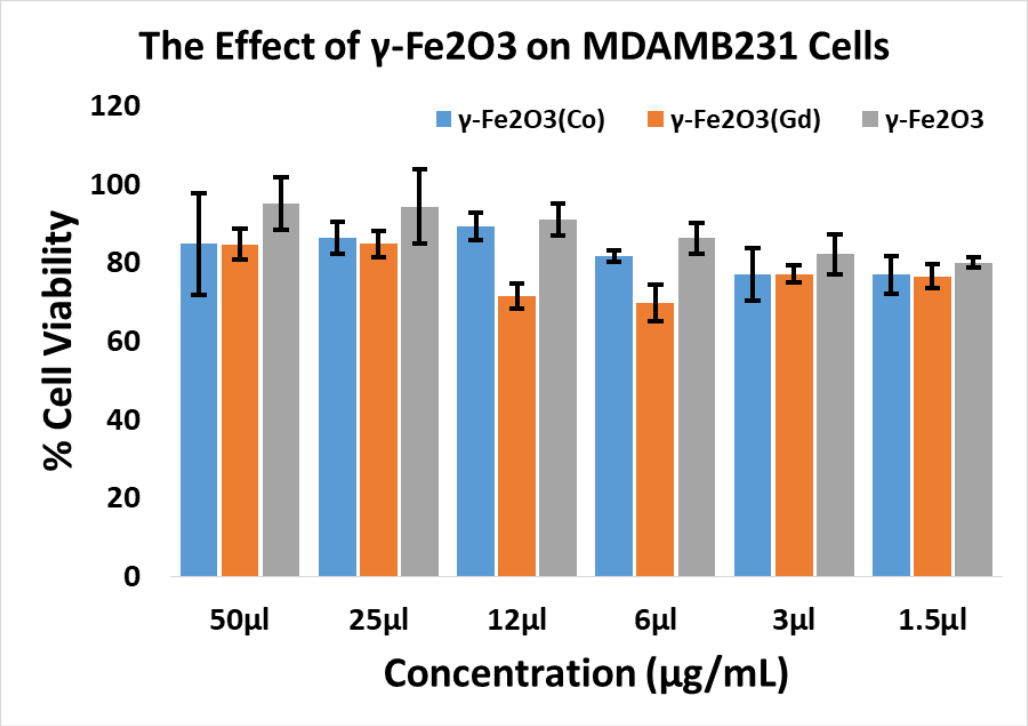

Fig. 7. MTT cell viability assay against MDA-MB-231 metastatic breast cancer cells incubated with different concentrations of γ-Fe_2O_3, γ-Fe_2O_3(Co-5%), and γ-Fe_2O_3(Gd-5%) MNPs. The

results clearly indicate the low toxicity of all tested γ-Fe2O3 NPs, and, thus, their safe utilization for MFH.

4. Conclusion

In conclusion, we reported a systematic study on the structural, DC, and AC magnetometry characterization of γ-Fe_2O_3, γ-Fe_2O_3(Gd-5%), and γ-Fe_2O_3(Co-5%) NPs. XRD, Rietveld and TEM analysis confirmed the phase purity and crystallite sizes of the as-prepared MNPs. DC and AC measurements indicated the superparamagnetic behavior of γ-Fe_2O_3, γ-Fe_2O_3 (Gd-5%) NPs and ferrimagnetic nature of γ-Fe_2O_3(Co-5%) NPs. Heating ability deduced from AC magnetometry measurements revealed the high heating efficiency and SAR value (120 W/g) of γ-Fe_2O_3(Co-5%), which is 6 times higher compared to γ-Fe_2O_3 or γ-Fe_2O_3(Gd-5%) NPs. This is mainly attributed to their higher effective anisotropy and saturation magnetization, where the heat dissipation in case of γ-Fe_2O_3(Co-5%) NPs is dominated by hysteresis losses, while that for γ-Fe_2O_3 or γ-Fe_2O_3(Gd-5%) NPs by Neel relaxation. Finally, cytotoxicity assay against metastatic breast cancer cells revealed that the samples exhibited minimal toxicity, even at relatively high concentrations (up to 500 µg/mL). Collectively our results indicate that Co-doped γ-Fe_2O_3 NPs hold great promise as a potential candidate for biomedical magnetic-mediated hyperthermia treatment.

Acknowledgements:

This work was supported and funded by the Deanship of Scientific Research at Imam Mohammad Ibn Saud Islamic University (IMSIU) (grant number IMSIU-RP23089).

References

[1] Jordan A, Wust P, Scholz R, et al. Magnetic Fluid Hyperthermia(MFH). In: U. H€afeli, W. Schutt, J. Teller, and M. Zborowski, editors, Scientific and clinical applications of magnetic carriers. Boston,MA: Springer US; 1997. pp. 569–595.

[2] W. Wu, C.Z. Jiang, V.A.L. Roy, Designed synthesis and surface engineering strategies of magnetic iron oxide nanoparticles for biomedical applications, Nanoscale. (2016). https://doi.org/10.1039/c6nr07542h.

[3] A.B. Salunkhe, V.M. Khot, S.H. Pawar, Magnetic Hyperthermia with Magnetic Nanoparticles: A Status Review, Curr. Top. Med. Chem. (2014). https://doi.org/10.2174/1568026614666140118203550.

[4] O.M.Lemine, Magnetic hyperthermia therapy using hybrid magnetic nanostructures,

Hybrid nanostructures for cancer theranostics, 20181, 25-138.

[5] De la Presa, P.; Luengo, Y.; Multigner, M.; Costo, R.; Morales, M.; Rivero, G.; Hernando, A. Study of heating efficiency as a function of concentration, size, and applied field in γ-Fe2O3 nanoparticles. The Journal of Physical Chemistry C 2012, 116, 25602-25610.

[6]. Lemine, O.; Omri, K.; Iglesias, M.; Velasco, V.; Crespo, P.; De La Presa, P.; El Mir, L.; Bouzid, H.; Yousif, A.; Al-Hajry, A. γ-Fe2O3 by sol–gel with large nanoparticles size for magnetic hyperthermia application. Journal of Alloys and Compounds 2014, 607, 125-131.

[7]. Martinez-Boubeta, C.; Simeonidis, K.; Makridis, A.; Angelakeris, M.; Iglesias, O.; Guardia, P.; Cabot, A.; Yedra, L.; Estradé, S.; Peiró, F. Learning from nature to improve the heat generation of iron-oxide nanoparticles for magnetic hyperthermia applications. Scientific reports 2013, 3, 1-8.

[8] El-Boubbou, K.; Lemine, O.M.; Ali, R.; Huwaizi, S.M.; Al-Humaid, S.; AlKushi, A. Evaluating magnetic and thermal effects of various Polymerylated magnetic iron oxide nanoparticles for combined chemo-hyperthermia. New Journal of Chemistry 2022, 46, 5489-5504.

[9] A. Aldaoud, O.M.Lemine, N.Ihzaz, L.El Mir, Sharif AbuAlrub, Kheireddine El-Boubbou, Magneto-thermal properties of Co-doped γ-Fe2O3 (γ-Fe2O3) nanoparticles for magnetic hyperthermia applications, Physica B: Condensed Matter, 639(2022), 413993

[10] Wang S-Y, Huang S, Borca-Tasciuc D-A. Potential sources of errors in measuring and evaluating the specific loss power of magnetic nanoparticles in an alternating magnetic field. IEEE Trans Magn. 2013;49(1):255–262

[11] Fortin J-P, Wilhelm C, Servais J, et al. Size-sorted anionic ironoxide nanomagnets as colloidal mediators for magnetic hyperthermia. J Am Chem Soc. 2007;129(9):2628–2635.

[12] Soetaert F, Kandala SK, Bakuzis A, et al. Experimental estimation and analysis of variance of the measured loss power of magnetic nanoparticles. Sci Rep. 2017;7(1):6661.

[13] Wildeboer RR, Southern P, Pankhurst QA. On the reliable measurement of specific absorption rates and intrinsic loss parameters in magnetic hyperthermia materials. J Phys D: Appl Phys. 2014; 47(49):495003.

[14] Bordelon DE, Cornejo C, Gruttner C, et al. Magnetic nanoparticle heating efficiency reveals magneto-structural differences when characterized with wide ranging and high amplitude alternating magnetic fields. J Appl Phys. 2011;109(12):124904.

[15] I. Rodrigo, I. Castellanos-Rubio, E. Garaio, O. K. Arriortua, M. Insausti, I. Orue, J. Á. García, and F. Plazaola, ‘‘Exploring the potential of the dynamic hysteresis loops via high field, high frequency and temperature adjustable AC magnetometer for magnetic hyperthermia characterization,’’ Int. J. Hyperthermia, vol. 37, no. 1, pp. 976–991, Jan. 2020

[16] I. Alotaibi, M.S. Alshammari, S. Algessair, N. Madkhali, N.A. All, M. Hjiri, S.A. Alrub, L. El Mir, O.M. Lemine, Synthesis, characterization and heating efficiency of Gd-doped γ-Fe2O3 (γ-Fe2O3) nanoparticles for hyperthermia application, Physica B: Condensed Matter. (2022).

[17] Juan A. Ramos-Guivar , Diego A. Flores-Cano and Edson Caetano Passamani Differentiating Nanomaghemite and Nanomagnetite andDiscussing Their Importance in Arsenic and Lead Removal from Contaminated Effluents: A Critical Review, Nanomaterials 2021, 11, 2310. https://doi.org/10.3390/nano11092310

[18] Lemine, O., Madkhali, N., Alshammari, M., Algessair, S., Gismelseed, A., Mir, L. E., Hjiri, M., Yousif, A. A. and El-Boubbou, K. 2021 Maghemite (γ-Fe2O3) and γ-Fe2O3-TiO2 nanoparticles for magnetic hyperthermia applications: Synthesis, characterization and heating efficiency. Materials 14 (19), pp. 5691.

[19] E. Abouzir, M. Elansary, M. Belaiche, et H. Jaziri, « Magnetic and structural properties of single-phase Gd 3+ -substituted Co–Mg ferrite nanoparticles », RSC Advances, vol. 10, no 19, p. 11244-11256, 2020, doi: 10.1039/D0RA01841D.

[20] Marin Tadic, Matjaz Panjan, Vesna Damnjanovic, Irena Milosevic, Magnetic properties of hematite (α-Fe2O3) nanoparticles prepared by hydrothermal synthesis method, Applied Surface Science 320 (2014) 183–187

[21] S. v. Komogortsev, R.S. Iskhakov, Law of approach to magnetic saturation in nanocrystalline and amorphous ferromagnets with improved transition behavior between power-law regimes, Journal of Magnetism and Magnetic Materials, 440, 15 (2017), Pages 213-216.

[22] Juan A. Ramos Guivar, M.A. Morales, F. Jochen Litterst, Suppression of exchange bias effect in maghemite nanoparticles functionalized with H2Y Journal of Magnetism and Magnetic Materials, Volume 420, 15 (2016), Pages 324-335

[23] Blomqvist L, Nordberg GF, Nurchi VM, Aaseth JO. Gadolinium in Medical Imaging-Usefulness, Toxic Reactions and Possible Countermeasures-A Review. Biomolecules. 2022 May 24;12(6):742. doi: 10.3390/biom12060742;

[24] Morales, I.; Costo, R.; Mille, N.; Da Silva, G.B.; Carrey, J.; Hernando, A.; De la Presa, P. High Frequency Hysteresis Losses on γ-Fe2O3 and Fe3O4: Susceptibility as a Magnetic Stamp for Chain Formation. Nanomaterials 2018, 8, 970. https://doi.org/10.3390/nano8120970

[25 Rogosnitzky M, Branch S. Gadolinium-based contrast agent toxicity: a review of known and proposed mechanisms. Biometals. 2016 Jun;29(3):365-76. doi: 10.1007/s10534-016-9931-7

[26] Juan A. Ramos-Guivar, Marco A. Morales , F. Jochen Litterst γ-Fe2O3 nanoparticles embedded in nanohydroxyapatite matrix for magnetic hyperthermia and in vitro osteoblast cell studies, Ceramics International

Volume 46, Issue 8, Part A, 1 June 2020, Pages 10658-10666
